Supporting Information

Binder-free MoSe/MMSe composite and onion-derived activated carbon electrode materials for high-performance hybrid supercapacitors

*Manchi Nagaraju, Bhimanaboina Ramulu, Ampasala Surya Kiran, and Jae Su Yu**

Department of Electronics and Information Convergence Engineering, Institute for Wearable Convergence Electronics, Kyung Hee University, 1732 Deogyeong-daero, Giheung-gu, Yongin-si, Gyeonggi-do 17104, Republic of Korea

*Corresponding author. Email address: jsyu@khu.ac.kr (J. S. Yu)

Section-I

1.1. Chemicals and materials

Magnesium nitrate hexahydrate ($Mg(NO_3)_2 \cdot 6H_2O$), ammonium molybdate tetrahydrate ($(NH_4)_6Mo_7O_{24} \cdot 4H_2O$), hydrochloric acid (HCl), urea (CH_4N_2O), and ammonium fluoride (NH_4F) were purchased from Sigma Aldrich Co., South Korea. Potassium hydroxide (KOH), ethylene glycol, and ethanol (C_2H_5OH) were obtained from Daejung Chemicals, South Korea. Nickel foam (NF), super-P carbon black, polyvinylidene fluoride (PVDF, $-(C_2H_2F_2)_n-$), and N-methyl-2-pyrrolidone (NMP, C_5H_9NO) were obtained from MTI Korea, South Korea. All the chemicals were of analytical grade and used directly without purification.

1.2. Material characterization techniques

Field-emission scanning electron microscope (FE-SEM, MERLIN (Carl Zeiss)) was used to examine the surface nanostructures of the prepared samples. Energy-dispersive X-ray (EDX) spectroscopy was used to observe the elements and their spread in the acquired morphology. The crystallinity and phase of the prepared materials were determined using X-ray diffraction (XRD, D8 Advance (Bruker)). High-resolution Raman spectroscopy (conducted via Raman microscopy) was used to investigate the vibration modes of the samples. A technique called X-ray photoelectron spectroscopy (XPS, K-alpha (Thermo Electron)) was used to examine the oxidation states of the sample components. Inductively coupled plasma spectroscopy (ICP, Direct Reading Echelle ICP, LEEMAN) analysis was performed. The transmission electron microscope (TEM, JEM 200CX, JEOL, 200 kV) was employed to investigate the intrinsic morphology of the obtained materials. The nitrogen (N_2) adsorption-desorption characteristics of all the prepared MoSe/MMSe, MoSe, MgSe, and OAC materials were explored on a BELSORP-max00131 surface area and porosity analyzer at 77 K and with the help of Brunauer-Emmett-Teller (BET) model. The specific surface areas of the MoSe/MMSe, MoSe,

MgSe, and OAC materials were measured, while the pore size distribution of the material was evaluated based on the BarrettJoyner-Halenda (BJH) theory.

Section-II

1.3. Electrochemical characterization techniques

The electrochemical properties of the prepared electrodes were evaluated using a three-electrode system equipped with an IviumStat electrochemical workstation. The active material loaded on the NF substrate served as the working electrode, the electrolyte was a 1 M KOH solution, a Pt wire served as the counter electrode, and Ag/AgCl served as the reference electrode. The slurry preparation process for the OAC/NF electrode is as follows. The OAC, PVDF, and super-P carbon black were mixed with the required amount of NMP at a weight ratio of 80:10:10 to create a slurry. The process took approximately 30 min to complete. The NF surface was then covered with a slurry in a 1 × 1 cm^2 region. The electrode was then dried for 12 h at 70 °C. Subsequently, it was compressed at a pressure of 10 MPa to ensure a secure bond between the active material and the NF. 3.1 mg cm^{-2} was recorded as the mass of the electrode over the NF.

The areal capacity (C_A), specific capacity (C_S), specific capacitance (C_{SC}), power density (P_d), and energy density (E_d) were calculated using the following formulae:S[1,3]

$$C_A = \frac{2I\int v(t)\,dt}{A \times V} \quad \text{(S1)}$$

$$C_S = \frac{2I\int v(t)\,dt}{m \times V} \quad \text{(S2)}$$

where C_A denotes the areal capacity (Ah cm^{-2}), C_{SC} denotes the specific capacity (mAh g^{-1}), I indicates the applied current (A), '$\int v(t)\,dt$' indicates the integral area of the discharge curve, A indicates the area (cm^2), V denotes the potential window (V), and m indicates the mass of the active electrode (g).

$$C_{SC} = \frac{I \times \Delta t}{m \times \Delta V} \quad \text{(S3)}$$

$$E_d = \frac{I \times \int v(t)\,dt}{m} \quad \text{(S4)}$$

$$P_d = \frac{E_d}{\Delta t} \quad \text{(S5)}$$

where C_{SC} denotes the specific capacitance (F g^{-1}), I indicates the applied current (A), 'm' is referred to as the mass of the active electrode (g), 'Δt' is referred to as the discharge time (s), 'ΔV' indicates the potential window (V), '$\int v(t)\,dt$' represents the integral area (cm^2), and 'E_d' and 'P_d' correspond to the energy density (Wh kg^{-1}) and power densities (W kg^{-1}), respectively.

The mass loadings of the positive (MoSe/MMSe/NF) and negative electrodes (OAC/NF) were estimated using the following well-known equation:

$$m_- = \frac{Q_+ \times a_+}{C_- \times \Delta V_-} \quad \text{(S6)}$$

where Q_+ and a_+ are the areal capacity (Ah cm^{-2}) and active area (cm^{-2}) of the positive electrode, respectively. ΔV_-, C_-, and m_- indicate the potential window (V), areal capacitance (F cm^{-2}), and mass (g) of the negative electrode, respectively.

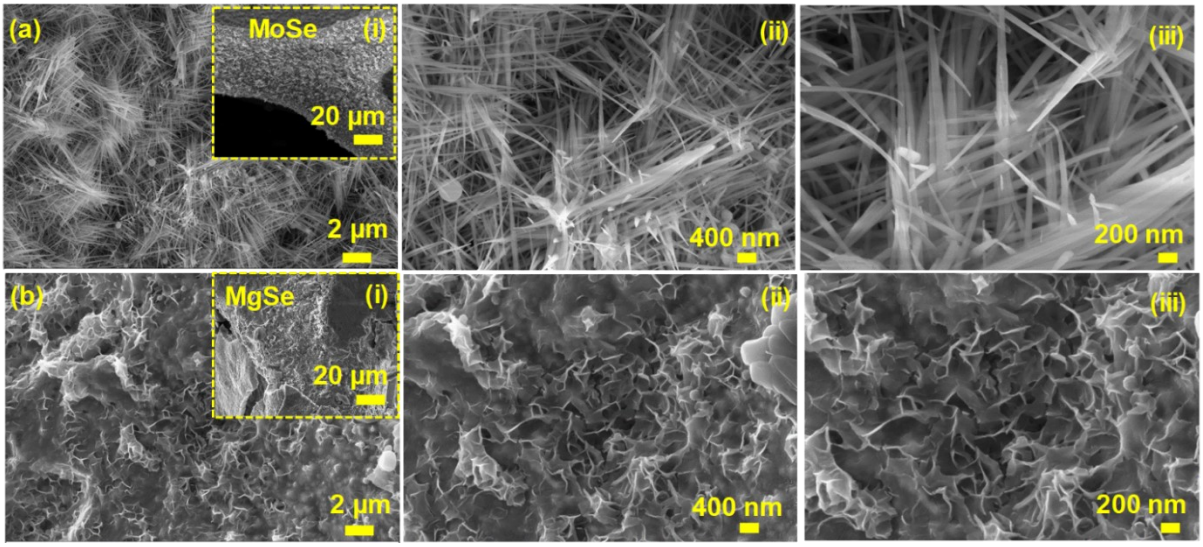

Fig. S1. Low- and high-magnification FE-SEM images of the (a)(i-iii) MoSe and (b)(i-iii) MgSe electrodes.

Using ICP analysis, the metal elemental ratio of the prepared MoSe/MMSe composite material was investigated, and the obtained values were plotted in the pie chart as shown in Fig. S4. The pie chart represented the elemental content of 93.81% (Mo), 4.49% (Mg), and 1.7% (Se). The optioned results were well-matched with the corresponding EDX and XPS analyses.

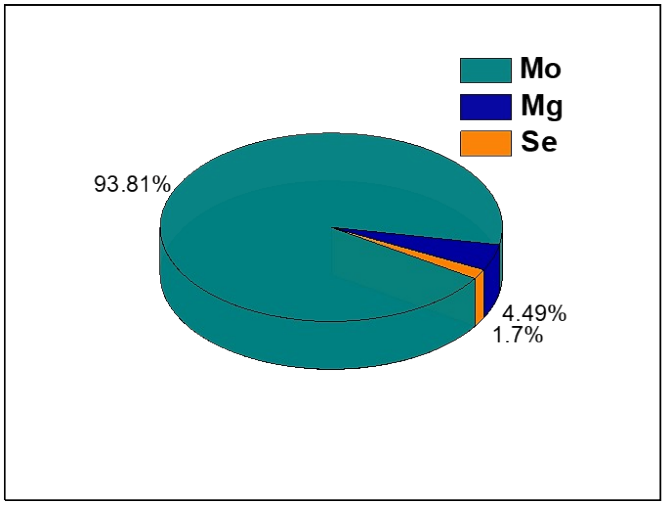

Fig. S2. ICP pie chart of the MoSe/MMSe composite material.

The pore size and surface area of the prepared MoSe/MMSe, MoSe, and MgSe composite materials were analyzed using Brunauer-Emmett-Teller (BET) and Barrett-Joyner-Halenda (BJH) analyses, as shown in Fig. S4. The N_2-sorption (adsorption/desorption) isotherm test was carried out under a liquid N_2 atmosphere, and the samples showed a type IV isotherm hysteresis loop, which signifies the typical mesoporous nature of the synthesized electrode materials. From the BET analysis, the specific surface area (SSA) values of the MoSe/MMSe, MoSe, and MgSe composite electrode materials were noticed to be 3.7 ± 0.5, 2.6 ± 0.5, and 1.6 ± 0.5 $m^2 g^{-1}$, respectively. Among them, the MoSe/MMSe composite material showed a higher SSA when compared to the MoSe and MgSe materials. The large SSA may be due to the hybrid morphology of nanospheres and nanowires and the synergistic effect between Na, Mg, and Se atoms in the MoSe/MMSe electrode. Moreover, the BJH analysis was used to determine the average pore diameter of all three electrodes, and the resultant plot is shown in the inset of Fig. S4. Herein, for the MoSe/MMSe electrode material, the major peak of the BJH pore size distribution curve was obtained at 1.7-2.2 nm, and for the MoSe and MgSe electrode materials, the major peak was noticed at 1.9-2.5 nm and 2-2.8 nm, respectively. The MoSe/MMSe composite electrode material having mesoporous nature with a large surface area exhibited enhanced electrochemical behaviors, providing numerous reactive sites for redox reactions and extensive pathways for electrolyte ions to penetrate. These observations suggest that the prepared electrode materials have the potential to offer high-rate capability and improved long-term stability.

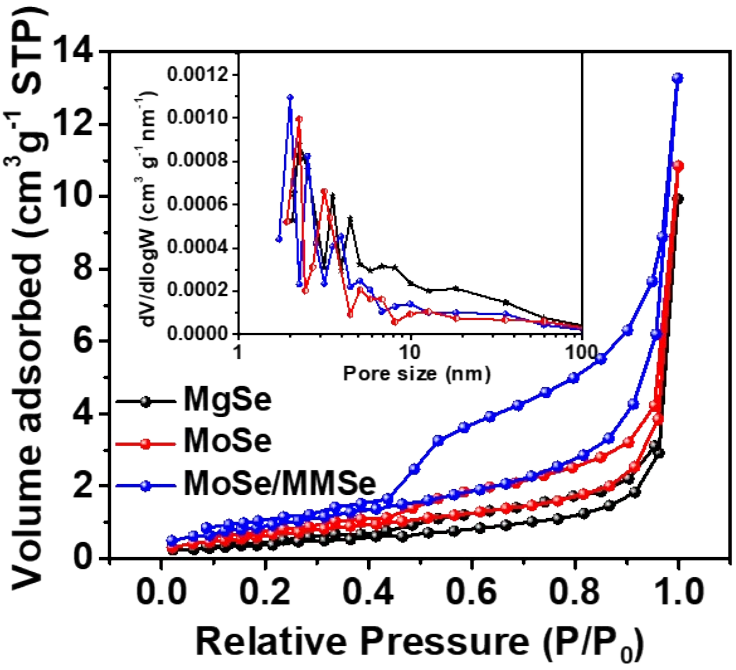

Fig. S3. N_2 adsorption and desorption isotherms of all the prepared materials.

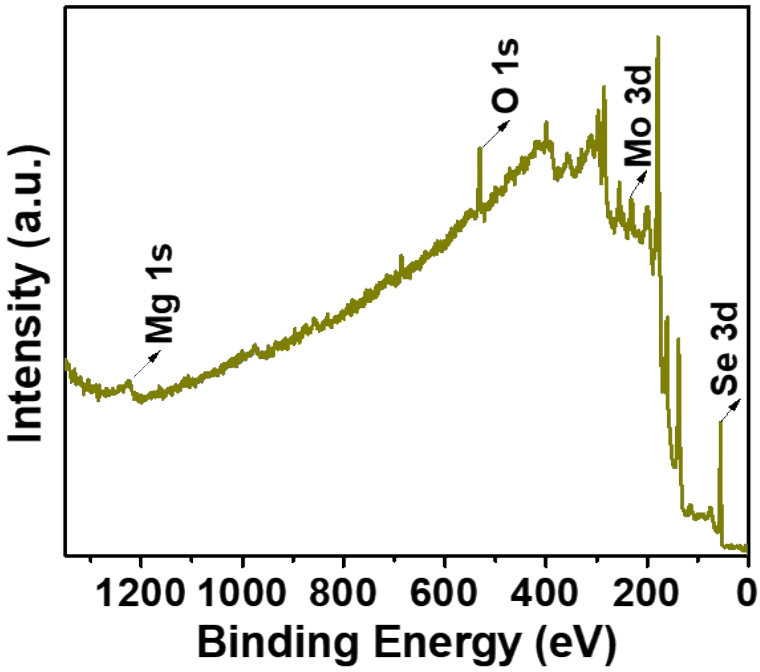

Fig. S4. Total XPS survey scan spectrum of the MoSe/MMSe composite material

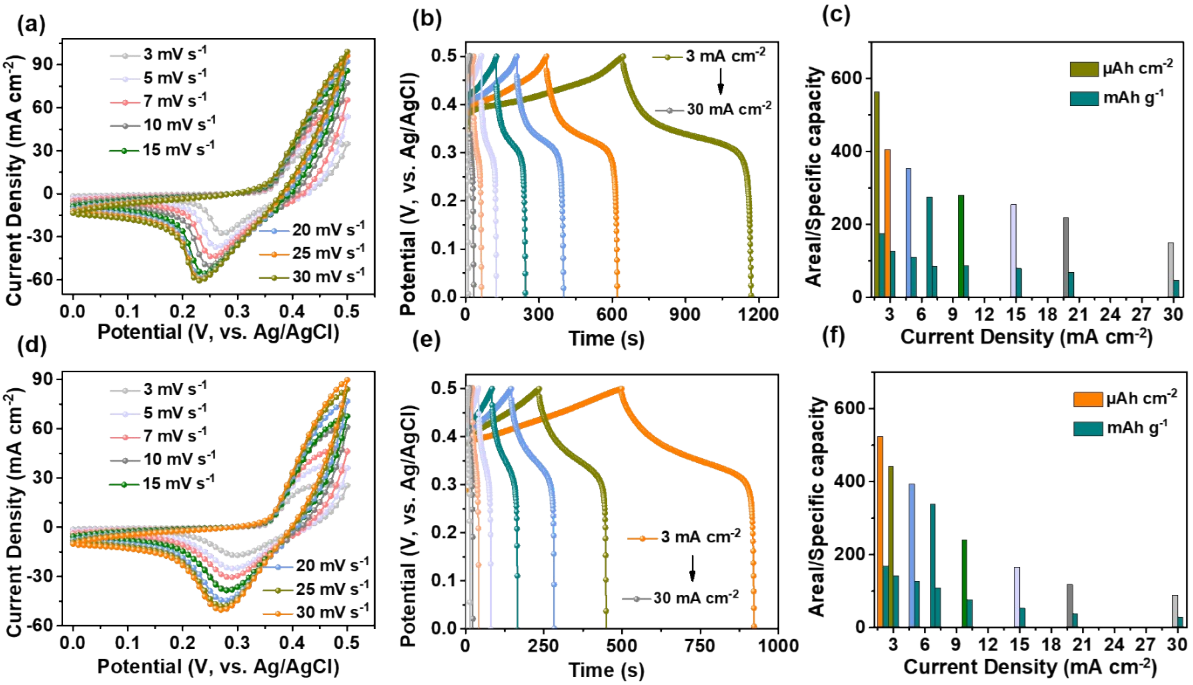

Fig. S5. (a) CV curves at various scan rates, (b) GCD curves at various current densities, and (c) C_A/Cs values for the MoSe electrode. (d) CV curves at various scan rates, (e) GCD curves at various current densities, and (f) C_A/Cs values for the MgSe electrode material.

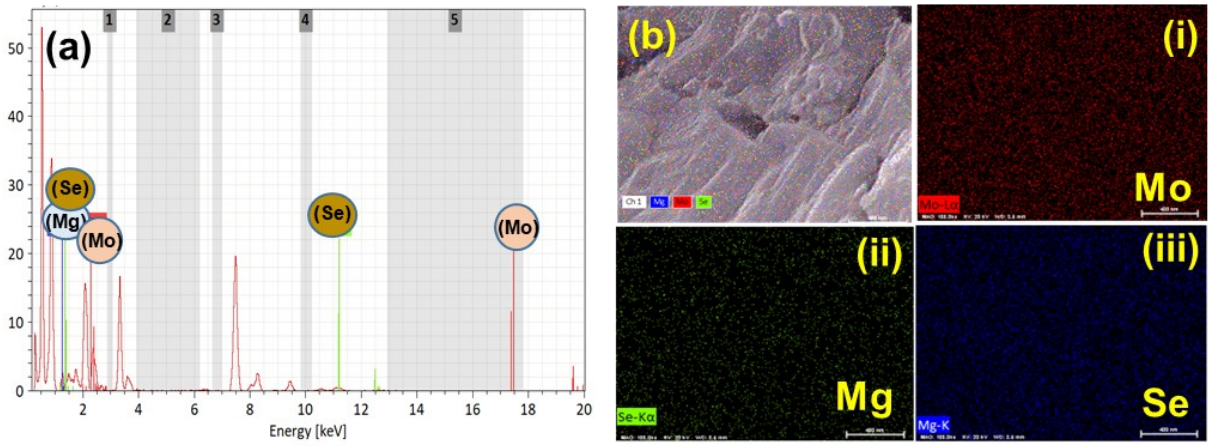

Fig. S6. (a) EDX spectrum (b) elemental mapping images of (i) Mo, (ii) Mg, and (iii) Se including layered electronic image for the MoSe/MMSe composite material after the cycling test.

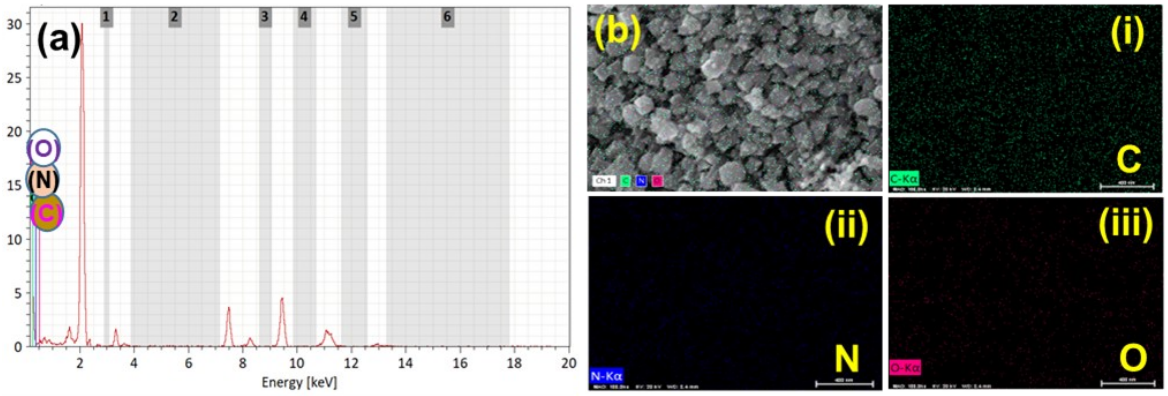

Fig. S7. (a) EDX spectrum (b) elemental mapping images of (i) C, (ii) N, and (iii) O including layered electronic image for the OAC material after the cycling test.

Table S1. Comparative electrochemical properties of our OAC electrode material with some recently reported biomass-derived SC electrode materials.

Biomass-derived carbons	**Electrolyte**	**Specific capacitance ($F\ g^{-1}$)**	**Ref.**
Onion	6 M KOH	127	S[4]
Onion	6 M KOH	423	S[5]
Onion	1 M Na_2SO_4	478	S[6]
Onion	6 M/L KOH	133.5	S[7]
Onion	3 M KNO_3	169	S[8]
Onion	2 M H_2SO_4	450	S[9]
Onion	**1 M KOH**	**940.6**	**Our work**

Table S2. Comparative E_d and P_d values and cycling stability of the MoSe/MMSe//OAC HSC cell with previously published reports.

Materials	**Electrolyte**	**Energy density (E_d)**	**Power density (P_d)**	**Durability test**	**Ref.**
Co/CVO/NF-80//AC	3 M KOH	26.1 Wh kg^{-1}	400 W kg^{-1}	5000 (83.4%)	S[3]
$NiCo_2S_4$/PPy//AC	3 M KOH	41.2 Wh kg^{-1}	402.2 W kg^{-1}	5000 (92.8%)	S[10]
CMS//AC	1 M KOH	18.6 Wh kg^{-1}	1938 W kg^{-1}	3000 (86.3%)	S[11]
Ni/$Ni_{0.8}Co_{0.2}Se$// AC	2 M KOH	17 Wh kg^{-1}	1526.8 W kg^{-1}	2000 (95%)	S[12]
$Ni_{0.9}Co_{1.92}Se_4$//AC	3 M KOH	26.2 Wh kg^{-1}	265 W kg^{-1}	-	S[13]
NiS/Mo_2S_{3-2}//AC	2 M KOH	31.2 Wh Kg^{-1}	850 W Kg^{-1}	10000 (81.3%)	S[14]
MoSe/MMSe//OAC	**1 M KOH**	**28.5 Wh kg^{-1}**	**2553.8 W kg^{-1}**	**45000 (74.3%)**	**Our work**

References

[S1] G. Nagaraju, S. C. Sekhar, B. Ramulu, S. K. Hussain, D. Narsimulu and J. S. Yu, *Nano-Micro Lett.* 2021, **13**, 1-18.

[S2] G. Nagaraju, S. C. Sekhar, B. Ramulu and J. S. Yu, *Energy Storage Mater.* 2021, **35**, 750-760.

[S3] X. Lv, W. Huang, J. Tang, L. Tang and Q. Shi, *Electrochim. Acta* 2021, **380**, 138248.

[S4] E. G. Shankar, A. K. Das and J. S. Yu, *J. Mater. Sci. Technol.* 2022, **125**, 118-127.

[S5] M. D. Mehare, A. D. Deshmukh and S. Dhoble, *J. Mater. Sci.* 2020, **55**, 4213-4224.

[S6] T. R. Kumar, R. A. Senthil, Z. Pan, J. Pan and Y. Sun, *J. Energy Storage* 2020, **32**, 101903.

[S7] A. Gopalakrishnan and S. Badhulika, *J. Energy Storage* 2021, **38**, 102533.

[S8] J. Xu, W. Zhang, D. Hou, W. Huang and H. Lin, *Chin. Chem. Lett.* 2017, **28**, 2295-2297.

[S9] S. Chaudhary, R. Mohan and O. Sinha, *Appl. Phys. A* 2020, **126**, 806.

[S10] J. Li, Y. Zou, B. Li, F. Xu, H. Chu, S. Qiu, J. Zhang, L. Sun and C. Xiang, *Ceram. Int.* 2021, **47**, 16562-16569.

[S11] M. Nagaraju, S. Chandra Sekhar, B. Ramulu, S. J. Arbaz and J. S. Yu, *J. Magnes. Alloys* 2022, **10**, 3565-3575.

[S12] K. Guo, S. Cui, H. Hou, W. Chen and L. Mi, *Dalton Trans.* 2016, **45**, 19458-19465.

[S13] W. An, L. Liu, Y. Gao, Y. Liu and J. Liu, *RSC Adv.* 2016, **6**, 75251-75257.

[S14] S. Wu, X. Yang, T. Cui, Q. Feng, S. Zhou, X. Xu, H. Zhao, L. Wu, Y. He and Q. Yang, *Colloids Surf. A: Physicochem. Eng. Asp.* 2021, **628**, 127332.